Chemistry—Methods

Research Article
doi.org/10.1002/cmtd.202400008

Chemistry Europe
European Chemical Societies Publishing

www.chemistrymethods.org

Orbi-SIMS Mediated Metabolomics Analysis of Pathogenic Tissue up to Cellular Resolution

Christine Kern,[a] Astrid Scherer,[a] Laura Gambs,[a] Mariia Yuneva,[b] Henning Walczak,[c, d] Gianmaria Liccardi,[e] Julia Saggau,[d, e] Peter Kreuzaler,*[f] and Marcus Rohnke*[a, g]

Tumors have a complex metabolism that differs from most metabolic processes in healthy tissues. It is highly dynamic and driven by the tumor cells themselves, as well as by the non-transformed stromal infiltrates and immune components. Each of these cell populations has a distinct metabolism that depends on both their cellular state and the availability of nutrients. Consequently, to fully understand the individual metabolic states of all tumor-forming cells, correlative mass spectrometric imaging (MSI) up to cellular resolution with minimal metabolite shift needs to be achieved. By using a secondary ion mass spectrometer (SIMS) equipped with an Orbitrap mass analyzer, we present a workflow to image primary murine tumor tissues up to cellular resolution and correlate these ion images with post acquisition immunofluorescence or histological staining. In a murine breast cancer model, we could identify metabolic profiles that clearly distinguish tumor tissue from stromal cells and immune infiltrates. We demonstrate the robustness of the classification by applying the same profiles to an independent murine model of lung cancer, which is accurately segmented by histological traits. Our pipeline allows metabolic segmentation with simultaneous cell identification, which in the future will enable the design of subpopulation-targeted metabolic interventions for therapeutic purposes.

Introduction

Altered metabolism has been regarded as a hallmark of cancer since the inception of molecular oncology, epitomized by Otto Warburg's ground-breaking observations linking oncogenic derailment to aerobic glycolysis, now referred to as the Warburg effect.[1] While many of the changes seen in tumors reflect the metabolic adaptations of healthy dividing cells,[1,2] the scale, synchronicity and persistence of growth in tumors does warrant its designation as an idiosyncratic metabolism different from any large scale metabolic program usually found in an adult organism. This is further compounded by the ephemeral nature of the tumor and its microenvironment, which is often impaired by an undersupply of both oxygen and nutrients due to poor vascularization.

Indeed, metabolic alterations have been the cornerstone of cancer diagnosis. In positron emission tomography (PET), the glucose analog fluorodeoxyglucose (FDG) is often used as a positron emitter.[3–7] The accumulation of FDG in tumors is based on the high metabolic rate and the dependency on glucose, which is at least partly due to the Warburg effect.[2,4,5] Magnetic resonance imaging (MRI) scans have been functionalized by the utilization of hyperpolarized stable isotope labeled metabolites such as pyruvate or glutamine, which allow the

[a] C. Kern, A. Scherer, L. Gambs, Prof. Dr. M. Rohnke
Institute of Physical Chemistry
Justus Liebig University Giessen
35392 Giessen, Germany
E-mail: Marcus.Rohnke@pc.jlug.de

[b] Dr. M. Yuneva
Oncogenes and Tumour Metabolism Laboratory
The Francis Crick Institute
London NW1 1 AT, UK

[c] Prof. Dr. H. Walczak
Centre for Cell Death, Cancer and Inflammation (CCCI)
UCL Cancer Institute
London WC1E 6DD, UK

[d] Prof. Dr. H. Walczak, J. Saggau
Institute of Biochemistry I & CECAD Cluster of Excellence
Medical Faculty
University of Cologne
50931 Cologne, Germany

[e] Dr. G. Liccardi, J. Saggau
Genome instability, inflammation and cell death laboratory
Institute of Biochemistry I
Centre of Biochemistry
Medical Faculty
University of Cologne
50931 Cologne, Germany

[f] Dr. P. Kreuzaler
University Hospital Cologne I & CECAD Cluster of Excellence
Medical Faculty
University of Cologne
50931 Cologne, Germany
E-mail: p.kreuzal@uni-koeln.de

[g] Prof. Dr. M. Rohnke
Center for Materials Research
Justus Liebig University Giessen
35392 Giessen, Germany

Supporting information for this article is available on the WWW under https://doi.org/10.1002/cmtd.202400008

visualization of the uptake and, to a certain extent, the utilization of these nutrients in vivo.[8–10]

While these imaging techniques are of the highest clinical value, they have a relatively low depth of information as they only highlight single predefined metabolic pathways. In order to address this problem, cancer tissues have been extensively studied using modern metabolomics.[11–13] Metabolomics, the global analysis of small molecule metabolites, can provide important information and new knowledge about the cancer state and the interaction of the metabolisms of cancer and non-cancer cells at cellular and/or systemic level.[11,14,15] With the help of modern metabolomics, for example, the importance of glutaminolysis for tumor growth[16–18] and de novo fatty acid biosynthesis for metastatic spread to certain organs such as the brain[17,19,20] has been highlighted. Analytical methods such as nuclear magnetic resonance spectroscopy (NMR) or mass spectrometry (MS) are primarily used for metabolomic studies in biological samples.[11,14,21] The advantages of NMR are its high reproducibility and the possibilities of quantifying metabolites and in vivo measurements.[11,12,14,21,22] The disadvantage is the low sensitivity, which is several orders of magnitude lower than in MS analyses.[11,14] In turn the advantage of MS methods such as gas chromatography (GC) MS or liquid chromatography (LC) MS, in addition to the high sensitivity, is the high mass resolution and mass accuracy.[11,12,14,23]

However, these methods often focus on the averaged metabolism of the heterogeneous cell populations of the tumor microenvironment (TME) and thus only provide data on the net metabolism of the entire cellular ensemble.[12] This inability to clearly observe metabolic reactions at a precise subcellular location, e.g., tumor cell area or areas within healthy tissue, is a major obstacle to understanding cell metabolism and how it changes in diseases such as cancer.[12] In an effort to disentangle the contribution of the different constituent cell types of the TME, analytical methods that simultaneously provide both chemical and spatial information are needed. Here, the emerging field of correlative mass spectrometric imaging (MSI) has proven to be a promising approach, in which MSI is superimposed and correlated with other imaging techniques such as light microscopy.[24–26]

In recent years, several MSI technologies have become established,[11,12,24,27–32] each with their own advantages and disadvantages. In all MSI technologies, there is usually a trade-off between spatial resolution, biological information, and tissue integrity. For example, matrix-assisted laser desorption ionization (MALDI) in combination with a time-of-flight (ToF) analyzer can reach a nominal lateral resolution of 10–20 μm and detect metabolites ranging from small molecules such as lactate to very large lipids of over 1000 Da.[27,31,33] By the dedicated combination of an atmospheric pressure (AP) MALDI setup and an Orbitrap mass analyzer, subcellular MSI with 1.4 μm lateral resolution with high mass resolution at the same time was demonstrated.[34] Nevertheless, the need to apply a matrix to the sample compromises multiple downstream modalities.[33–35] Desorption electrospray ionization (DESI) MSI is a somewhat newer development, which allows imaging of the same range of metabolites as MALDI-ToF, but with minimal damage to the tissue, thus readily allowing correlative imaging of the same tissue in different modalities.[27,28,30,31] Lateral resolution, however, is only around 20 μm[35] and does not allow imaging of single cells. To overcome this problem, DESI-MSI was recently combined with CLEIM-iT (correlative light, electron, and ion microscopy in tissues), a technology that is based on detection of a stably labeled tracer molecule and allows subcellular detection.[36] The reliance on a clearly defined tracer, however, limits the range of potential applications. Some groups have instead resorted to indirect measurement of metabolic activity by quantifying key metabolic enzymes using mass cytometry.[37–40] While this technology is valuable for historical clinical samples, it is inherently indirect and therefore prone to error.

In order to investigate pathogenic tissue and differentiate their heterogeneous cell populations from another, methods providing higher spatial resolution in combination with high mass resolution are required. Secondary ion mass spectrometry (SIMS) is a surface analysis method that overcomes several pitfalls seen in other modalities. It is based on secondary ions (SIs) generated from a primary ion beam, is tracer- and matrix-free, and can reach a lateral resolution of 50 nm or less. Therefore, it enables analysis of tissue samples at single-cell level.[41–45] However, a disadvantage of ToF-SIMS analyses of tumor tissues is that, for example, the use of the bismuth liquid metal ion gun (LMIG) as the primary ion source, standardly used in many studies,[32,41,46–50] can lead to excessive fragmentation of the analytes during ionization. In addition, the mass resolving power of the ToF analyzer of SIMS instruments is limited ($m/\Delta m \sim 30{,}000$).[51,52] These drawbacks make it difficult to accurately identify the original molecule that generated the corresponding secondary ion, and thus limiting the amount of detailed information about the metabolic landscape.[52] To reduce fragmentation of metabolites, an argon gas cluster ion beam (GCIB) with large Ar_x^+ clusters as primary ion species can be used instead of LMIG to release large biomolecules from samples.[43,52–54] To overcome the disadvantages of mass resolution, SIMS can also be combined with an Orbitrap analyzer (Orbi-SIMS) instead of a ToF analyzer.[51–61] The use of the Orbitrap mass analyzer combines the strengths of high mass resolution ($>240\,000$ at m/z 200), high mass accuracy (<1 ppm) and high-resolution SIMS imaging with spatial resolution down to 2 μm in Orbi-SIMS analyses.[53,62] This makes Orbi-SIMS ideal for precise signal identification at single cell level and offers a new level of metabolite analysis.

Here, we present a workflow to perform correlative imaging of both murine breast and lung tumors utilizing an Orbi-SIMS imaging set-up with a nominal resolution inferior to the size of single cells. By performing downstream microscopy analysis including fluorescent microscopy and histological staining, we can benchmark our tissue segmentation and prove that Orbi-SIMS analysis allows an unsupervised segmentation of different TME components such as the tumor cells, immune cells and stromal areas.

Research Article
doi.org/10.1002/cmtd.202400008
Chemistry Europe
European Chemical Societies Publishing

Results and Discussion

Orbi-SIMS Imaging of Murine Breast Tumors

In order to benchmark the Orbi-SIMS to image tumor tissues and their TME, we chose a reductionist approach (Figure 1). We used a variation of a previously established murine breast cancer model.[63,64] Here, tumors are driven by the mammary specific oncogene MMTV-Wnt1,[65] but are concomitantly marked with red fluorescence by the inclusion of an mTmG-cassette, which expresses tdTomato under the constitutive Rosa26 promoter (Cre mediated recombination leads to expression of eGFP, but no recombination was carried out in this manuscript).[66] As the tumors were generated by serial transplant, the resulting animals present with tdTomato positive tumor cells, while all remaining cells of the TME have no fluorescence. For tumor analysis, one part of the tissue was analyzed by LC–MS after methanol/chloroform-based lipid extraction as previously described,[64] while the other part was sectioned for imaging analysis with Orbi-SIMS and fluorescence microscopy and histological staining (workflow in Figure 1). For correlative imaging, previous tissue sections of the breast tumor were fluorescently stained with CD45, a pan-immune cell marker, and analyzed by fluorescence microscopy. This enabled the selection of suitable ROIs, which included distinct morphological features of tumor cells, the immune compartment, and stromal tissue, for the subsequent tissue section to be analyzed by MSI.

The Orbi-SIMS mass spectra were compared with the LC–MS data (Figure 1e), while the MS images were correlated with the fluorescence images (Figure 1f). In contrast to the breast tumor sections, lung tumor sections were not stained with fluorescence but rather immunohistochemically in first test measurements. Orbi-SIMS imaging of tumor sections were performed in both positive and negative ion mode, with measurements in negative ion mode resulting in spectra that were far richer in significant peaks. In particular, cancerous tissue was poorly detected in the positive ion mode. Therefore, all Orbi-SIMS results presented here are based on measurements in negative ion mode.

Comparing an RGB overlay of single ion images (Figure 1f) with the fluorescence image of the consecutive tissue section, we noticed very clear regional differences, with certain ions almost perfectly tracking the tumor margins (red color in fluorescence image and Orbi-SIMS overlay), while others were accumulated in stromal areas (black color in fluorescence microscopy, blue color in Orbi-SIMS overlay). A third class of mass signals more closely tracked the immune cell signal (yellow color in both fluorescence and Orbi-SIMS image), albeit with some overlap with tumor tissue. We therefore conclude

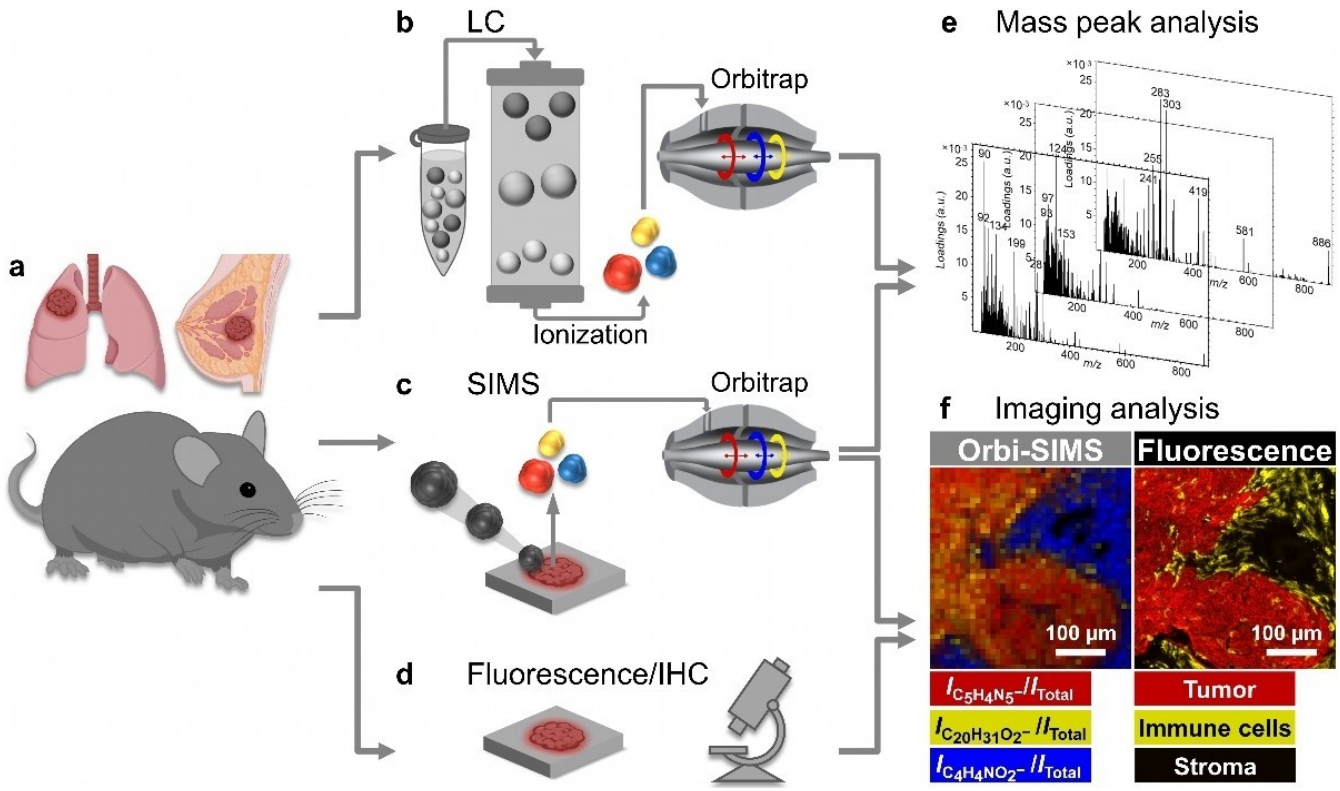

Figure 1. General workflow to perform correlative imaging of a) murine breast and lung tumors. (b) LC–MS and c) Orbi-SIMS analysis are performed for e) mass peak analysis. f) Correlative imaging analysis is done by c) Orbi-SIMS imaging and d) microscopy of fluorescence and immunohistochemical staining of the tumor tissue sections. In the fluorescence image, tumor tissue is shown in red, immune cells in yellow and stromal tissue in black. In the Orbi-SIMS overlay image, tumor tissue is depicted in red by adenine ($C_5H_4N_5^-$ at *m/z* 134.0473), immune cells in yellow by FA(20:4) ($C_{20}H_{31}O_2^-$ at *m/z* 303.2328), and stromal tissue in blue by $C_4H_4NO_2^-$ (*m/z* 98.0240). All individual secondary ion images were normalized to total ion image prior to overlay. Orbi-SIMS images were taken in negative ion mode with 20 keV Ar_{3000}^+ clusters as primary ion species.

Research Article
doi.org/10.1002/cmtd.202400008
Chemistry Europe
European Chemical Societies Publishing

that the regional prevalence of certain metabolites is closely linked to the underlying tissue type. The morphology of the MSI data clearly fits to the one of the consecutive fluorescence images even though the fluorescence images belong to the consecutive sections.

A R-based code was used to compare the Orbi-SIMS data with the LC–MS data. Peaks with a deviation of 15 ppm were considered a match, excluding duplicate hits. The peak comparison showed that 182 peaks could be found with both LC–MS and Orbi-SIMS (Figure 2a). In total, there are more mass signals in LC–MS spectra (1087 peaks) than in Orbi-SIMS spectra (749 peaks), which might be due to the fact that LC–MS shows a better sensitivity due to the analysis of digested tissue. In addition, the analyte is preconcentrated in LC–MS.

The modest overlap of LC–MS and Orbi-SIMS data is probably due to the higher fragmentation in the Orbi-SIMS, while the fragmentation is minimal during LC–MS. This would be confirmed by the fact that the average *m/z* in the LC–MS data is significantly higher than in the Orbi-SIMS data (*m/z* 574 vs *m/z* 262). A comparison of the 182 metabolites found both with LC–MS and Orbi-SIMS (Figure 2b) shows that 76 of them are lipid fragments, 31 peaks could be assigned to nucleotide fragments, 46 peaks originate from organic components and 29 peaks are species such as phosphates or sulphur species. In conclusion, most major metabolite classes can be found in our Orbi-SIMS analysis. Due to fragmentation, Orbi-SIMS will in many cases be able to identify the compound class, rather than the specific compound, which is important to keep in mind in downstream analysis, but does not hamper biological conclusions on the basis of compound-class distributions.

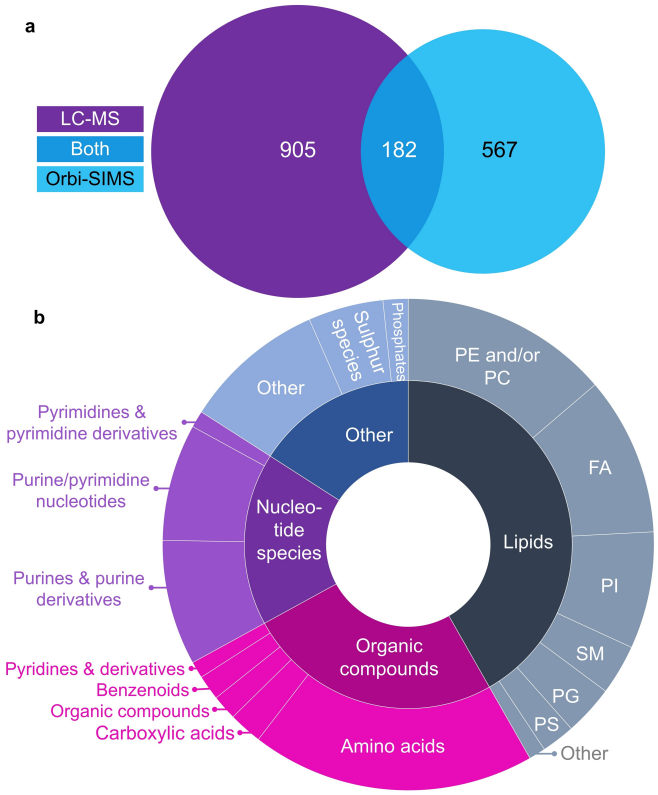

Figure 2. a) Venn diagram comparing the number of mass peaks found by Orbi-SIMS and LC–MS analysis, illustrating that 182 compounds were common to both analysis methods, while 567 were unique to Orbi-SIMS and 905 were unique to LC–MS. b) Classes of metabolites common in Orbi-SIMS and LC–MS.

Since the data evaluation of Orbi-SIMS mass spectra, which contain the masses of all molecular and elemental SIs detected during a measurement, is very complex, we applied multivariate statistical analysis (MVSA) in the form of multivariate curve resolution (MCR) in the next step of data evaluation. This method reduces the complexity of the data set and can reveal correlation or dependency structures between variables.[51] MCR uses a non-negativity constraint that forces all components to be positive. Thus, MCR analysis provides component spectra that look like conventional mass spectra and are therefore easier to interpret.[67–69] Since the number of components to be calculated must be determined in advance and thus some kind of initial estimate of the components must be made, MCR is considered a guided method. Here, our initial estimate was based on the PCA results of the datasets.[67–69] The complete Orbi-SIMS mass list used for all MCR analyses can be found in Table S1.

Figure 3 shows an example of the MCR analysis of an Orbi-SIMS measurement of a murine breast tumor. As a result of the PCA analyzes carried out previously, the MCR analyzes were carried out with 5–7 factors, with ultimately three factors being able to clearly distinguish different areas of the TME. The respective mass spectra of these three factors show the metabolic profiles of different areas of the examined tissue (Figure 3a). Projection of the MCR factors (Figure 3b) onto the tissue section reveals a clear correlation between the fluorescence and MSI data, which allowed us to assign the spatial distribution of MCR factor 1 to tumor tissue (Fig. 3c), MCR factor 2 to stromal cells, and MCR factor 5 to immune cells.

The identified MCR factors were then used as starting point to manually create the metabolic profiles for tumor, immune, and stromal cells. For that, it was examined in which factors individual peaks have the highest loading intensity. For example, the mass peak at *m/z* 303.2328 appears to be significant for several factors (Figure 3, Figure S2). However, if one compares the intensity of this peak within the various factors (Figure S2) as well as the secondary ion image with the mass image of the factor for immune cells, it is clear that this peak can be assigned to the factor for immune cells. In this way, all MCR factors were checked and the mass peaks were assigned to the different areas of the tumor. The final mass list of the metabolites responsible for the tumor factor can be found in table S2, for the stroma factor in table S3, and for the immune cell factor in table S4.

We applied the three metabolic profiles to additional murine breast tumors (Figure 4). For this purpose, the peaks from the mass lists of Tables S2–4, which represent the metabolic profiles of the tumor, immune and stromal tissue, were summed up in each case. The resulting ion images are displayed in overlays (Figure 4c, d, f, g, j, k) and compared with the fluorescence images of the consecutive tumor section (Figure 4a, b, e, h, i). Again, the Orbi-SIMS images of these metabolic profiles agree very well with the fluorescence

Research Article
doi.org/10.1002/cmtd.202400008
Chemistry Europe
European Chemical Societies Publishing

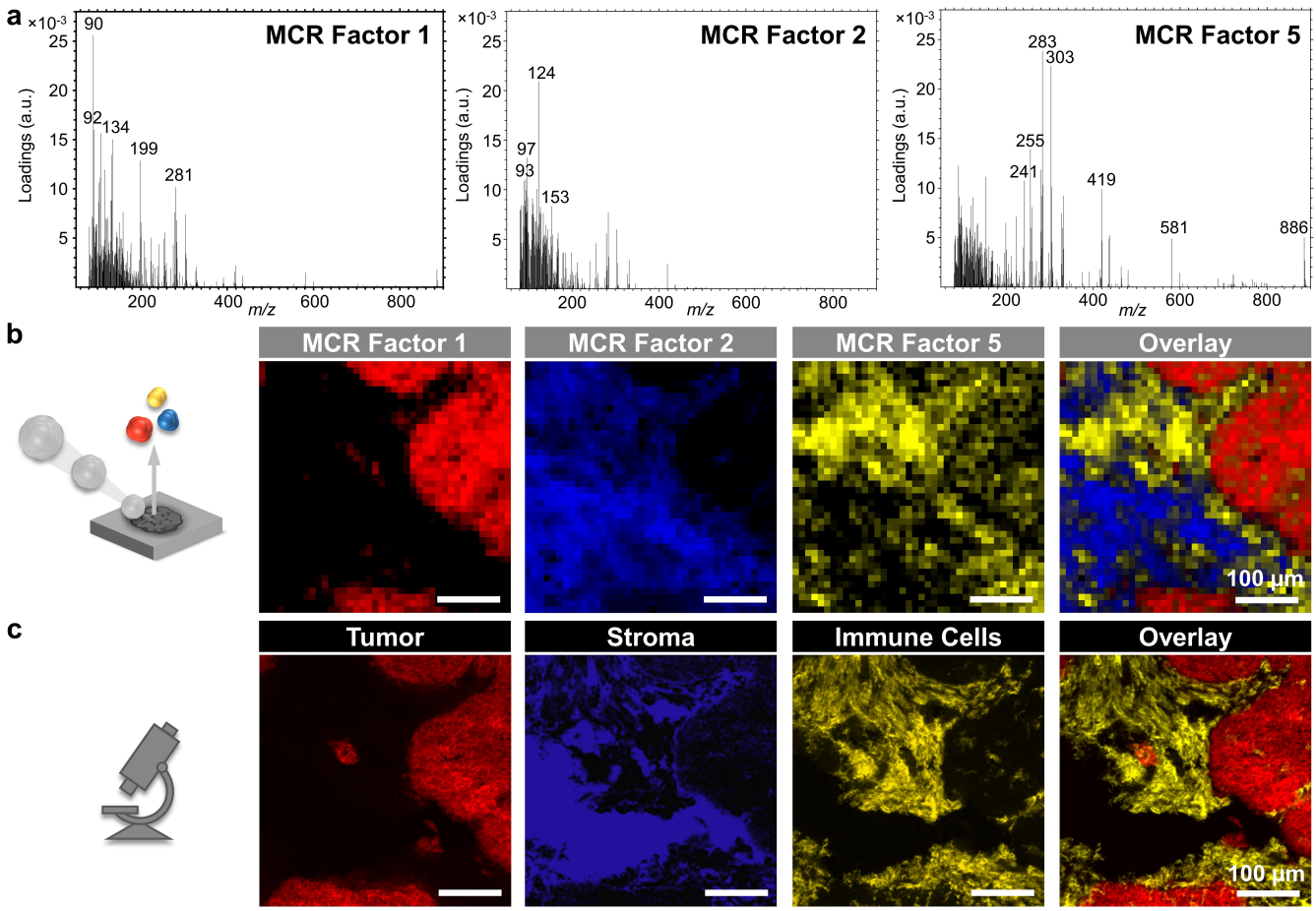

Figure 3. MCR analysis of Orbi-SIMS data of murine breast tumor. (a) Mass peaks for MCR factors 1, 2, and 5 show the metabolic profiles of different areas of tumor tissue. (b) Orbi-SIMS images show the spatial distribution of the metabolite profiles of MCR factors 1, 2, and 5. Here, MCR factor 1 is shown in red, MCR factor 2 in blue, and MCR factor 5 in yellow. (c) In fluorescence images, tumor tissue is shown in red, immune cells in yellow and stromal tissue in blue (no color (black) in the overlay image). The comparison of the Orbi-SIMS images with the corresponding fluorescence images shows that tumor tissue can be visualized with MCR factor 1, stroma cells with MCR factor 2 and immune cells with MCR factor 5. Orbi-SIMS images were taken in negative ion mode with 20 keV Ar_{3000}^+ clusters as primary ion species (pixel size: 10 µm, spot size: 2 µm). All secondary ion images were normalized to total ion image.

staining, with slight deviations since the fluorescence images show the consecutive sections. A detailed similarity analysis of the images based on mean squared error (MSE) and structural similarity index (SSIM) values is given in the SI, Figure S6. In total, 19 Orbi-SIMS measurements were performed on five different tumor tissue sections of murine breast tumors. In all these measurements, tumor tissue could be distinguished from immune cells and stromal cells by using the metabolic profiles. This demonstrates the robustness of our correlative imaging approach. We thus conclude that Orbi-SIMS imaging with 20 keV Ar_{3000}^+ clusters as primary ion species in negative ion mode enables the segmentation of different cell populations in tumor sections.

Next, we took a closer look at the metabolic profiles in a compound class analysis (Figure 5).

Tumor tissue: We found 119 mass peaks that determine the metabolic profile of the tumor cells. 25 of these peaks were also detected with LC–MS, and a further five peaks represent isotopes of the jointly detected mass peaks, which were only measured with Orbi-SIMS (Table S2, Figure 5a, b–e). The most intense peaks to characterize the cancerous tissue were found to be nucleotide fragments such as $C_4N_3^-$ (*m/z* 90.0096), $C_4H_2N_3^-$ (*m/z* 92.0253), $C_4H_2N_4^-$ (*m/z* 106.0285), $C_4H_3N_4^-$ (*m/z* 107.0363), $C_5HN_4^-$ (*m/z* 117.0200), $C_5HN_4O^-$ (*m/z* 133.0150), and $C_5H_4N_5^-$ (*m/z* 134.0473). Especially fragments of purines adenine and guanine characterize tumor cells the most. Purines are essential components of nucleotides as well as energy carriers and necessary for cell proliferation, which, when drastically increased, is a hallmark of cancer. Increased purine levels in tumor tissue in connection with increased nucleic acid levels has been reported for cancer tissue since the 1930s.[70,71] Moreover, the purine metabolism has been the target of potential cancer therapy approaches for several decades and is still a promising field of research.[72–76] Using Orbi-SIMS imaging, we can demonstrate that tumor cells can be detected and distinguished from other cell populations primarily through increased signal intensities of nucleotide fragments.

Immune cells: Overall, in areas of immune cells, we were able to determine 200 peaks with Orbi-SIMS measurements in negative polarity, 56 of which we also found in LC–MS measurements, and further 10 peaks represent isotopes of those peaks (Table S4, Figure 5a, f–i). The most dominant

Research Article
doi.org/10.1002/cmtd.202400008
Chemistry Europe
European Chemical Societies Publishing

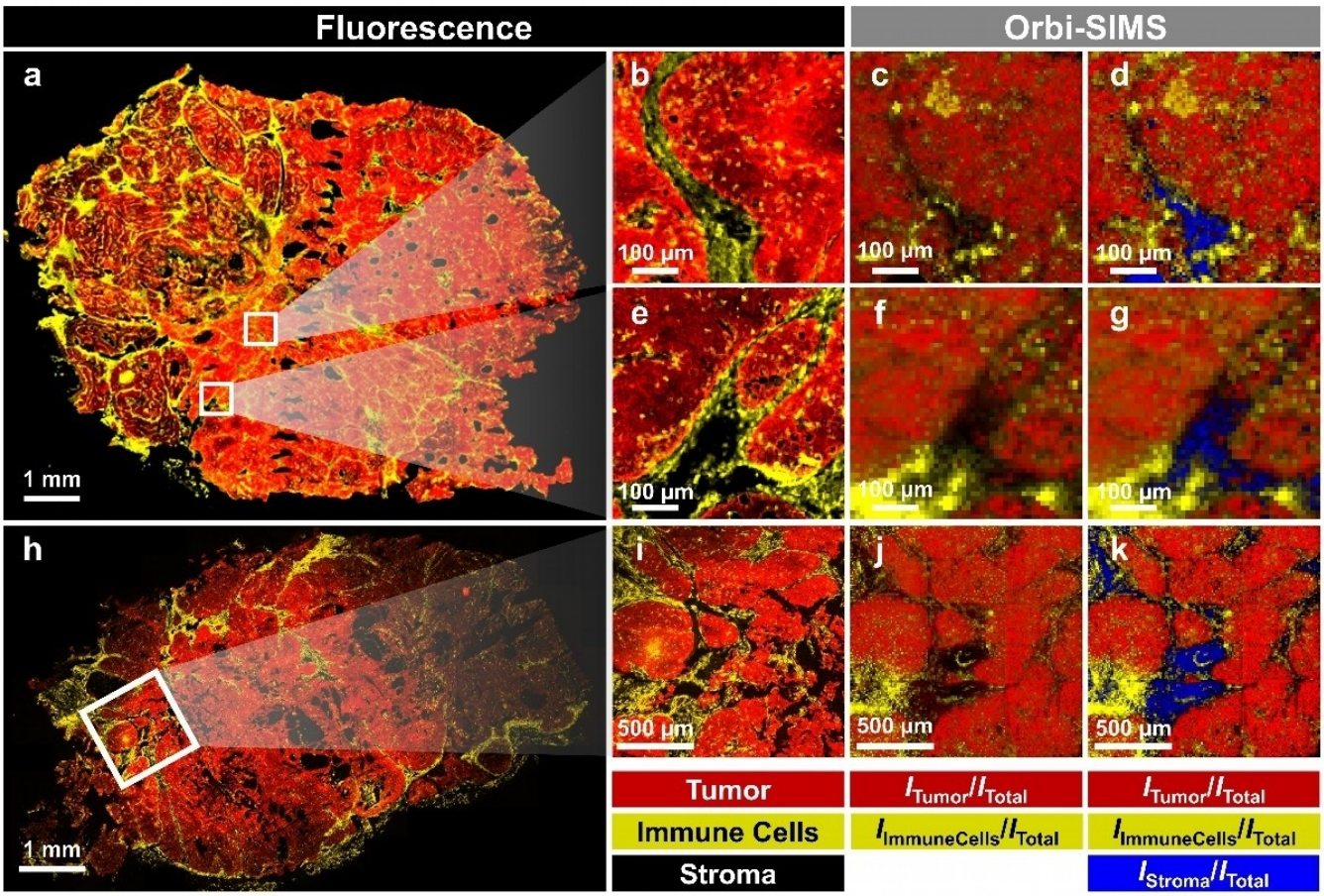

Figure 4. Orbi-SIMS images of different murine breast tumors correlated to fluorescence images. a) Fluorescence images of a murine breast tumor section. b, e) Detailed fluorescence images with c, d) and f, g) corresponding Orbi-SIMS overlay images of the consecutive tissue section (pixel sizes: 6 µm). h) Fluorescence image of a tumor tissue section of a different murine breast tumor with h) a detailed image and j, k) the corresponding Orbi-SIMS overlay images of the consecutive tumor section (pixel size: 10 µm). For the Orbi-SIMS images, the summed peak lists (Tables S2–4) of the respective metabolic profiles of tumor cells, immune cells, and stromal cells were used. In the Orbi-SIMS overlay images, tumor tissue is depicted in red, immune cells in yellow, and non-cancerous stromal tissue in blue. In fluorescence images, tumor tissue is shown in red, immune cells in yellow and stromal tissue in black. Orbi-SIMS images were taken in negative ion mode with 20 keV Ar_{3000}^+ clusters as primary ion species (spot size for all: 2 µm). All secondary ion images were normalized to total ion image prior to overlay.

compounds to characterize the immune cells were fragments of fatty acids and lipids, originating from lipid species including lysophosphatidic acids (LPA), lysophosphatidylcholines (LPC), lysophosphatidylethanolamines (LPE), phosphatidic acids (PA), phosphatidylcholines (PC), phosphoethanolamines (PE), phosphatidylglyceroles (PG), phosphatidylinositoles (PI), phosphatidylserines (PS), as well as phosphosphingolipids (SM). Lipid compounds found in our samples have also been observed in immune cells in various studies using Orbi-SIMS analysis, supporting our observations.[53,59,61] Lipids are important components of the cell membrane and key molecules for improving our understanding of metabolic pathways.[77,78] The main components of the lipid bilayer of cells are phospholipids, i.e. the lipid species that we have mainly detected in immune cells, e.g., PC ($C_4H_{11}NPO_4^-$ at *m/z* 168.0428), LPE ($C_{23}H_{47}O_6NP^-$ at *m/z* 464.3144), and PI (PI(38:4) $C_{47}H_{82}O_{13}P^-$ at *m/z* 885.5489, loss of arachidonic acid at *m/z* 581.3093, inositol head group $C_6H_{10}PO_8^-$ at *m/z* 241.0119). Furthermore, fatty acid fragments, such as $C_{12}H_{23}O_2^-$ (*m/z* 199.1702), FA(16:0) ($C_{16}H_{31}O_2^-$ at *m/z* 255.2329), FA(18:1) ($C_{18}H_{33}O_2^-$ at *m/z* 281.2486), and FA(18:0) ($C_{18}H_{35}O_2^-$ at *m/z* 283.2642), showed high intensity in regions of immune cells. While there are multiple possible metabolites in the case of unsaturated fatty acids and the possibility of the detected ions resulting from phospholipid fragmentation,[61] it is likely that FA(20:5) ($C_{20}H_{29}O_2^-$ at *m/z* 301.2173), FA(20:4) ($C_{20}H_{31}O_2^-$ at *m/z* 303.2328) and FA(20:3) ($C_{20}H_{33}O_2^-$ at *m/z* 305.2486) can be labeled as arachidonic acid which is required for prostaglandin biosynthesis. Prostaglandins are known to be part of the immune system's inflammatory response and elevated immune cell derived prostaglandin levels have been associated with cancer in previous studies.[79,80]

Stromal cells. For non-cancerous stromal cells, we found 71 mass peaks with Orbi-SIMS, 26 of which we were also able to detect with LC–MS (Table S3, Figure 5a, j–m). Most of the peaks responsible for the metabolic profile of stromal cells can be assigned to amino acids (e.g., $C_3H_3O_3^-$ at *m/z* 87.0080, $C_3H_6NO_2^-$ at *m/z* 88.0396, $C_4H_4NO_2^-$ at *m/z* 98.0240, or Taurine fragment $C_2H_6SNO_3^-$ at *m/z* 124.0068). Stromal cells are an important cell

Research Article
doi.org/10.1002/cmtd.202400008

Chemistry Europe
European Chemical Societies Publishing

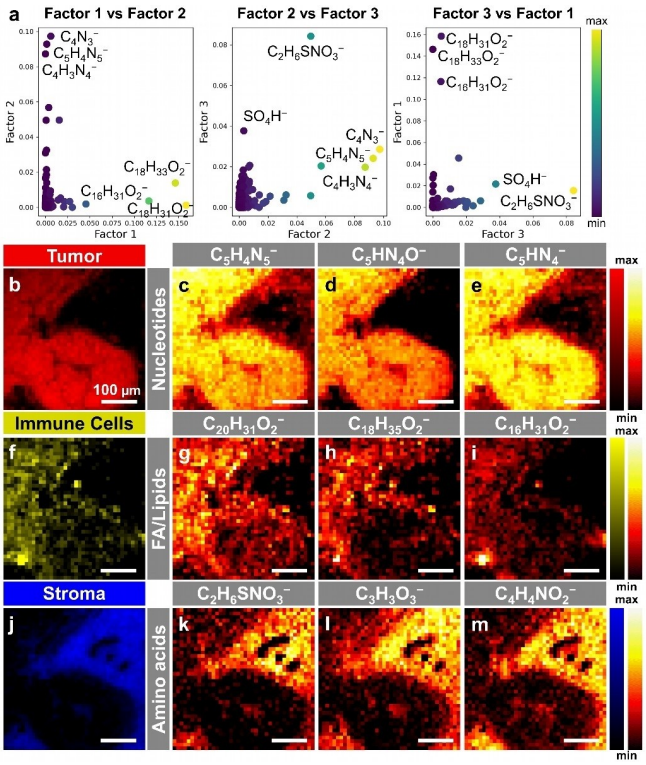

Figure 5. Compound class analysis of Orbi-SIMS spectra and imaging analysis. (a) Plots of the crosswise correlated factors 1–3 are shown, with the ions with the highest values for each axis being displayed. Factor 1 shows the metabolic profile of immune cells (summed peaks of Table S4), factor 2 of tumor cells (summed peaks of Table S2), and factor 3 of stromal cells (summed peaks of Table S3). (b)–(e) Spatial distribution of tumor cells which are mostly characterized by nucleotide fragments (e.g., $C_5HN_4^-$ at *m/z* 117.0200, $C_5HN_4O^-$ at *m/z* 133.0150, $C_5H_4N_5^-$ at *m/z* 134.0473). (f)–(i) Immune cells are mostly characterized by fatty acid or lipid fragments (e.g., $C_{16}H_{31}O_2^-$ at *m/z* 255.2329, $C_{18}H_{35}O_2^-$ at *m/z* 283.2642, $C_{20}H_{31}O_2^-$ at *m/z* 303.2328). (j)–(m) Stroma cells are mostly characterized by mass fragments of amino acids (e.g., $C_3H_3O_3^-$ at *m/z* 87.0080, $C_4H_4NO_2^-$ at *m/z* 98.0240, $C_2H_6SNO_3^-$ at *m/z* 124.0068). Orbi-SIMS images were taken in negative ion mode with 20 keV Ar_{3000}^+ clusters as primary ion species (pixel size: 10 µm, spot size: 2 µm). All secondary ion images were normalized to total ion image.

population in the TME. They can be recruited by cancer cells and play a fundamental role in the metabolism, development, growth, and spread of tumors as well as resistance to therapy.[81–85] Recruited stromal cells, also called tumor-associated stromal cells (TASCs), include mesenchymal stem cells (MSCs), tumor-associated adipocytes (TAAs), cancer-associated fibroblasts (CAFs) or tumor endothelial cells (TECs).[82,83,85] Unlike normal stromal cells, which undergo a reversible activation process upon acute injury or inflammatory processes, TASCs are chronically activated by tumor cell activity and show lower contractility, higher survival potential, and higher proliferation.[84,85] They are able to maintain tumor growth by expressing a higher number of proteins and mobilizing free amino acids, which they make available to the tumor cells to cover their increased metabolic needs and thus support tumor development.[82,84,85] Since we detected mainly amino acid mass signals at high intensity in the area of the stromal cells, this may be an indication that these are activated stromal cells, which can actively contribute to the metabolism and growth of tumors. However, we were not able to distinguish different TASCs from one another, for example by detecting cell-specific Orbi-SIMS mass signals. Furthermore, CAFs are known to remodel the ECM, for example by secreting proteinases,[86] thus we currently cannot exclude that some free amino acids might be the result of enzymatic digestion.

Besides amino acid signals, mass fragments such as $C_3H_5O_3^-$ at *m/z* 89.0237, which may originate from lactic acid, for example, and sulphur species such as SO_3H^- (*m/z* 80.9644) or SO_4H^- (*m/z* 96.9594), were also detected in stromal cell areas. Lactic acid is important for the energy requirements of stromal cells, but can also act as a signaling molecule.[82,87] Lactic acid can shuttle between different cell populations within the TME and enables interaction between tumor and stromal cells, which can induce metabolic reprogramming of stromal cells to TASCs.[82,87] The high mass intensity of a lactic acid fragment in areas of the stromal cells is another indicator that we were able to detect TASCs using Orbi-SIMS measurements. The detected sulphur species may originate both from amino acids such as taurine and from proteoglycans (PGls).[88–90] PGls are structural molecules located primarily in the extracellular matrix (ECM). They are necessary for the correct ECM conformation and provide the tissue with structural integrity.[88–90] PGs regulate cell-cell and cell-ECM interactions as well as the activity of signaling pathways and critical interactions in the TME.[88–90] Both tumor cells and TASCs are involved in the reorganization of the ECM and thus the PGls, favouring tumor growth, migration and invasion.[88–90]

Orbi-SIMS Imaging of Murine Lung Tumors

To further evaluate the general applicability of our Orbi-SIMS based classification method, we opted to apply the same metabolic profiles to an independent murine model of small cell lung cancer (SCLC) (Figure 6, Figures S3–4). SCLC was induced by administration of an adenovirus that carried the Cre recombinase (Ad-Cre) to eight week old RP mice, thus inactivating both p53 and Rb.[91] Orbi-SIMS imaging of the lung tissue sections was carried out with 20 keV Ar_{3000}^+ clusters as primary ion species in negative ion mode under cryogenic conditions, i.e. the same experimental approach as the Orbi-SIMS measurements of the murine breast tumors. In total, five Orbi-SIMS measurements of two different lung tumor sections were performed. As the lung tumor sections lack endogenous fluorescence, we opted to stain the lungs via IHC to reveal the CD45-positive immune cells, whilst gaining insights into tissue histology.

The spatial representation of the metabolic profiles, which we determined using the Orbi-SIMS analyzes of the breast tumors (Tables S2–S4), also lead to a clear distinction between tumor cells, immune cells, and stromal cells in murine lung tumors (Figure 6b–e, g–j). The metabolic profiles evaluated in this study can therefore also be applied to other types of tumors and enable segmentation into different cell subpopulations of the TME. Interestingly however, not all structures could be correctly assigned. The most prominent was the so-called

Research Article
doi.org/10.1002/cmtd.202400008
Chemistry Europe
European Chemical Societies Publishing

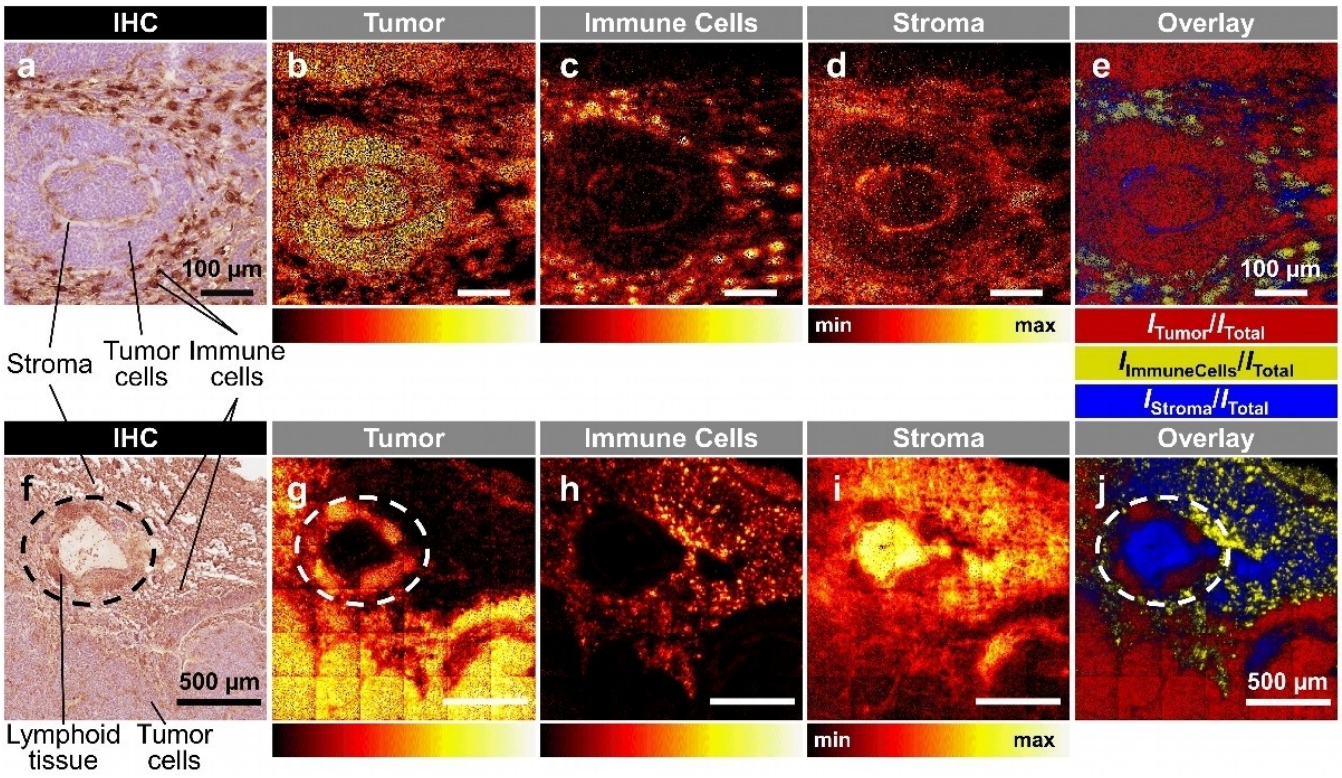

Figure 6. Microscopy images of IHC staining of two different murine SCLC tissue sections compared to the corresponding Orbi-SIMS images. (a), (f) In IHC staining, immune cells are depicted as reddish-brown dots, stromal tissue is shown in white-brownish color, and tumor cells are shown in light-purple color. (b)–(d) and (g)–(i) Orbi-SIMS images of SCLC tissue sections show the spatial distribution of the metabolic profiles of tumor cells, immune cells and stromal tissue. (e), (j) In the Orbi-SIMS overlay images, tumor tissue is depicted in red, immune cells in yellow, and stromal tissue in blue. (f) Besides areas of tumor, immune, and stromal cells, bronchus associated lymphoid tissue is also visible with IHC staining (encircled area). (g) In the Orbi-SIMS image, the same mass fragments (metabolic profile) depict tumor cells and lymphoid tissue, which are therefore not distinguishable (encircled area shows lymphoid tissue). Orbi-SIMS images were taken in negative ion mode with 20 keV Ar_{3000}^+ clusters as primary ion species (spot size: 2 µm). b–e) Pixel size: 2 µm. g–j) Pixel size: 4 µm. All secondary ion images were normalized to total ion image.

bronchus-associated lymphoid tissue (BALT), which typically surrounds the pulmonary bronchioles (Figure 6f–j, Figures S3–4). BALTs are almost entirely constituted by immune cells, such as T cells, B cells or dendritic cells, and consequently stain positive for the pan-immune cell marker CD45 (Figure 6f, Figures S3–4). The Orbi-SIMS derived metabolic profile, however, is indistinguishable from that of tumor tissue (Figure 6g–j, Figures S3–4). No mass fragments could be found that could specifically represent only the lymphatic tissue, which means that the BALT region cannot be segmented by our MSI method. This highlights how crucial the correlative aspect of our analysis is, in order to avoid misannotation of tissues.

Conclusions

In this study, we present a workflow to perform correlative imaging of different kinds of murine tumors utilizing an Orbi-SIMS imaging set-up down to nominal subcellular resolution in combination with downstream microscopy analysis including fluorescent microscopy and histological staining. Overall, with our proof-of-concept study we were able to show that the use of Orbi-SIMS for image analysis of tumor tissue represents a new possibility for untargeted metabolomics of pathogenic tissue. Our analysis strategy enabled the characterization of the tumor microenvironment and histopathological features with minimal sample preparation, high sensitivity, as well as high spatial and mass resolution, which are difficult to simultaneously achieve with other analysis platforms. We have shown that TME cell subpopulations have distinct metabolite profiles and that the metabolite profiles highlighted in breast tumors are also transferable to lung tumor samples. This suggests that metabolic characterization of tumor tissue using cryogenic Orbi-SIMS analysis should be considered as a valuable analytical method in future studies.

In this work, MSI carried out with an Orbi-SIMS provided not only clear distinction between tumor and immune cells but also stromal cells in both small and large area imaging. With Orbi-SIMS imaging, we found that specifically nucleotide peaks allow a neat differentiation between cancer and other cancer associated cell types. This ability to assess nucleotide metabolism in tumor cells could lead to the identification of metabolic pathways that can be used to develop effective cancer therapeutics. Furthermore, we were able to determine that amino acid signals were primarily detected (upregulated) in stromal cells. The explanation for this could be that the stromal cells measured here are tumor-associated stromal cells, which support tumor development in the TME by providing free

amino acids. However, we were unable to distinguish different TASCs from each other, but only distinguished stromal cells from tumor cells and immune cells. Finally, we were able to determine lipid and fatty acid peaks as metabolites that can be used to represent immune cells and distinguish them from other tissue types. Here, especially fatty acid signals from arachidonic acid as well as mass fragments from phospholipids such as PIs, LPEs and PC showed high mass signal intensity.

Overall, high-resolution mass spectrometric metabolite imaging by Orbi-SIMS showed that it is able to largely distinguish pathological proliferation from normal cell growth. Importantly, our pipeline allows metabolic segmentation with correlative cell identification, a prerequisite for the development of subpopulation-targeted metabolic interventions for therapeutic purposes. However, it should also be mentioned that a limiting step of Orbi-SIMS image analysis is the analysis speed. For example, it takes about 18 hours to record a (1.5×1.5) mm^2 image with a pixel size of 4 μm and would therefore result in a low sample throughput.

Several challenges remain, and will need to be addressed, as we refine the method. For example MS/MS analysis of selected mass fragments will need to be done, e.g., to investigate whether arachidonic acid signals originate from free arachidonic acid or from phospholipid fragmentation. In order to reduce overall fragmentation, different Ar_x^+ cluster sizes and their influence on fragmentation can also be examined in future experiments. Lastly, integration with multiplex antibody-based methods such as mass cytometry can be added correlatively post-MSI for precise single cell identification of immune cells and CAF subtypes.

Supporting Information

The authors have cited additional references within the Supporting Information. Data that support the findings of this study are available in the supplementary material of this article.

Acknowledgements

MR and CK thank the DFG for funding the Hybrid-SIMS (M6, IONTOF GmbH, Münster, Germany) under grant number INST 162/544-1 FUGG. All authors thank Pascal Dippel for his support with Orbi-SIMS data analysis.

Conflict of Interests

The authors declare no conflict of interest.

Data Availability Statement

The data that support the findings of this study are available from the corresponding author upon reasonable request.

Keywords: Orbi-SIMS · Metabolomics · Mass Spectrometric Imaging · Tumor Microenvironment · Single Cell Resolution

[1] O. Warburg, F. Wind, E. Negelein, *J. Gen. Physiol.* **1927**, *8*(6), 519–30.
[2] T. Hodgkinson, et al., *Sci. Adv.* **2021**, *7*(9), eabb7921.
[3] S. Peppicelli, et al., *Theranostics* **2020**, *10*(7), 2944–2948.
[4] G. Zhang, et al., *J. Nucl. Med.* **2015**, *56*(4), 607–612.
[5] M. W. N. Nijsten, G. M. van Dam, *Med. Hypotheses* **2009**, *73*(1), 48–51.
[6] C. K. Hoh, *Nucl. Med. Biol.* **2007**, *34*(7), 737–742.
[7] P. Lindholm, et al., *J. Nucl. Med.* **1993**, *34*(1), 1–6.
[8] S. H. Jørgensen, et al., *Semin. Nucl. Med.* **2022**, *52*(3), 374–381.
[9] A. Cho, et al., *J. Nucl. Med.* **2017**, *58*(8), 1201–1206.
[10] E. B. Adamson, et al., *Phys. Med. Biol.* **2017**, *62*(13), R81.
[11] A. K. Kaushik, R. J. DeBerardinis, *Biochim. Biophys. Acta* **2018**, *1870*(1), 2–14.
[12] V. Ruiz-Rodado, A. Lita, M. Larion, *Nat. Methods* **2022**, *19*(9), 1048–1063.
[13] L. Puchades-Carrasco, et al., *Oncotarget* **2016**, *7*(11).
[14] E. G. Armitage, C. Barbas, *J. Pharm. Biomed. Anal.* **2014**, *87*, 1–11.
[15] N. J. Serkova, K. Glunde, *Metabolomics of Cancer, in Tumor Biomarker Discovery: Methods and Protocols*, M. A. Tainsky, Editor. 2009, Humana Press: Totowa, NJ. 273–295.
[16] J. M. Matés, et al., *Semin. Cell Dev. Biol.* **2020**, *98*, 34–43.
[17] A. Hirayama, et al., *Cancer Res.* **2009**, *69*(11), 4918–4925.
[18] J. W. Erickson, R. A. Cerione, *Oncotarget* **2010**, *1*(8), 734–40.
[19] R. Pandey, et al., *Mol. Carcinog.* **2017**, *56*(11), 2355–2371.
[20] G. B. Ferraro, et al., *Nature Cancer* **2021**, *2*(4), 414–428.
[21] D. R. Schmidt, et al., *CA Cancer J Clin* **2021**, *71*(4), 333–358.
[22] K. A. Vermeersch, M. P. Styczynski, *J. Carcinog.* **2013**, *12*, 9.
[23] K. A. Kouremenos, M. Johansson, P. J. Marriott, *J. Cancer* **2012**, *3*, 404–420.
[24] X. Ma, F. M. Fernández, *Mass Spectrom. Rev.* **2022**, *e21804a*: e21804.
[25] J. M. Neumann, et al., *J. Cancer Res. Clin. Oncol.* **2022**, *148*(2), 351–360.
[26] M. Tuck, et al., *Front. Chem.* **2022**, *10*.
[27] M. Planque, et al., *Curr. Opin. Chem. Biol.* **2023**, *76*, 102362.
[28] C. Sun, et al., *Proc. Natl. Acad. Sci. USA* **2019**, *116*(1), 52–57.
[29] K. Vijaya Lakshmi, *Spatial Metabolomics Using Imaging Mass Spectrometry, in Metabolomics: Recent Advances and Future Applications*, V. Soni, T. E. Hartman, Editors. 2023, Springer International Publishing: Cham. 423–477.
[30] M. Sans, et al., *Cancer Res.* **2017**, *77*(11), 2903–2913.
[31] M. J. He, et al., *Front. Oncol.* **2022**, *12*.
[32] T. Hu, et al., *Nat. Commun.* **2023**, *14*(1), 8260.
[33] M. K. Andersen, et al., *Cancer & Metabolism* **2021**, *9*(1), 9.
[34] M. Kompauer, S. Heiles, B. Spengler, *Nat. Methods* **2017**, *14*(1), 90–96.
[35] J. Han, et al., *TrAC Trends Anal. Chem.* **2019**, *112*, 13–28.
[36] A. Fearns, et al., *PLoS Biol.* **2021**, *18*(12), e3000879.
[37] T. Van Acker, et al., *Anal. Chim. Acta* **2019**, *1074*, 43–53.
[38] Y. J. Wang, et al., *Cell Metab.* **2016**, *24*(4), 616–626.
[39] S. C. Bendall, et al., *Science* **2011**, *332*(6030), 687–696.
[40] F. J. Hartmann, et al., *Nat. Biotechnol.* **2021**, *39*(2), 186–197.
[41] S. K. Gularyan, et al., *Mol. Cell. Proteomics* **2020**, *19*(6), 960–970.
[42] K. Dimovska Nilsson, et al., *Biointerphases* **2020**, *15*(4).
[43] T. B. Angerer, et al., *Anal. Chem.* **2016**, *88*(23), 11946–11954.
[44] J. Brison, et al., *Surf. Interface Anal.* **2011**, *43*(1–2), 354–357.
[45] J. S. Fletcher, et al., *Rapid Commun. Mass Spectrom.* **2011**, *25*(7), 925–932.
[46] M. A. Robinson, et al., *Biointerphases* **2015**, *11*(2).
[47] J.-W. Park, et al., *Appl. Surf. Sci.* **2008**, *255*(4), 1119–1122.
[48] Y. L. Cintron-Diaz, et al., *Analyst* **2020**, *145*(21), 7056–7062.
[49] J. Park, et al., *Biointerphases* **2018**, *13*(3).
[50] B. M. Bluestein, et al., *Biointerphases* **2018**, *13*(6).
[51] C. Kern, et al., *Biointerphases* **2023**, *18*(4).
[52] W. He, et al., *Anal. Chem.* **2023**, *95*(14), 5994–6001.
[53] M. K. Passarelli, et al., *Nat. Methods* **2017**, *14*(12), 1175–1183.
[54] A. M. Kotowska, et al., *Nat. Commun.* **2020**, *11*(1), 5832.
[55] C. Kern, et al., *Analyst* **2022**, *147*(18), 4141–4157.
[56] C. L. Newell, et al., *Angew. Chem. Int. Ed.* **2020**, *59*(41), 18194–18200.
[57] J. Zhang, et al., *Anal. Chem.* **2020**, *92*(13), 9008–9015.
[58] F. Linke, et al., *Acta Neuropathologica Communications* **2023**, *11*(1), 6.
[59] W. Suvannapruk, et al., *Bio Protoc* **2023**, *13*(15), e4727.
[60] L. Matjacic, et al., *Surf. Interface Anal.* **2022**, *54*(4), 331–340.
[61] W. Suvannapruk, et al., *Anal. Chem.* **2022**, *94*(26), 9389–9398.
[62] S. Van Nuffel, et al., *Anal. Chem.* **2020**, *92*(17), 12079–12087.
[63] P. Kreuzaler, et al., *Proc. Natl. Acad. Sci. USA* **2019**, *116*(44), 22399–22408.

Research Article
doi.org/10.1002/cmtd.202400008

[64] P. Kreuzaler, et al., *Nature Metabolism* **2023**, *5*(11), 1870–1886.
[65] A. S. Tsukamoto, et al., *Cell* **1988**, *55*(4), 619–625.
[66] M. D. Muzumdar, et al., *Genesis* **2007**, *45*(9), 593–605.
[67] D. J. Graham, L. J. Gamble, *Biointerphases* **2023**, *18*(3).
[68] D. J. Graham, D. G. Castner, *Mass Spectrom.* **2013**, *2(Spec Iss)*, S0014.
[69] D. J. Graham, D. G. Castner, *Biointerphases* **2012**, *7*(1), 49.
[70] H.v. Euler, G. Schmidt, *Biol. Chem.* **1934**. *223*(5–6), 215–228.
[71] M. E. Lombardo, J. J. Travers, L. R. Cerecedo, *J. Biol. Chem.* **1952**, *195*(1), 43–48.
[72] W. B. Parker, *Chem. Rev.* **2009**, *109*(7), 2880–2893.
[73] J. Yin, et al., *Front. Immunol.* **2018**, *9*, 1697.
[74] E. S. Ali, I. Ben-Sahra, *Trends Cell Biol.* **2023**, *33*(11), 950–966.
[75] H.-I. Wu, et al., *J. Hematol. Oncol.* **2022**, *15*(1), 45.
[76] N. J. Mullen, P. K. Singh, *Nat. Rev. Cancer* **2023**, *23*(5), 275–294.
[77] B. Alberts, et al., *Ann. Bot.* **2003**, *91*, 401.
[78] S. G. Ostrowski, et al., *Anal. Chem.* **2005**, *77*(19), 6190–6196.
[79] J. Watson, et al., *Br. J. Cancer* **2019**, *120*(11), 1045–1051.
[80] A. M. Hendrick, M. D. Mitchell, A. L. Harris, *Eur. J. Cancer Clin. Oncol.* **1988**, *24*(6), 1069–1071.
[81] P. W. Tang, et al., *Am. J. Physiol. Cell Physiol.* **2023**, *325*(3), C731–C749.
[82] D. Niu, et al., *Int. Immunopharmacol.* **2022**, *106*, 108597.
[83] Y. Zhao, et al., *Cell Death Dis.* **2023**, *14*(9), 587.
[84] M. Reina-Campos, J. Moscat, M. Diaz-Meco, *Curr. Opin. Cell Biol.* **2017**, *48*, 47–53.
[85] K. M. Bussard, et al., *Breast Cancer Res.* **2016**, *18*(1), 84.
[86] K. Wright, et al., *Cancers (Basel).* **2023**, *15*(6).
[87] S. Romero-Garcia, et al., *Front. Immunol.* **2016**, *7*.
[88] M. Mellai, et al., *Chondroitin Sulphate Proteoglycans in the Tumour Microenvironment*, in *Tumor Microenvironment : Extracellular Matrix Components – Part B*, A. Birbrair, Editor. 2020, Springer International Publishing: Cham. 73–92.
[89] G. Tzanakakis, et al., *Cancers* **2020**, *12*(9), 2401.
[90] J. Clegg, et al., *Front. Cell Dev. Biol* **2020**, *8*.
[91] R. Meuwissen, et al., *Cancer Cell* **2003**, *4*(3), 181–189.

Manuscript received: May 24, 2024
Version of record online: July 12, 2024